ELSEVIER

Contents lists available at ScienceDirect

Acta Materialia

journal homepage: www.elsevier.com/locate/actamat



Solid-solution and precipitation softening effects in defect-free faceted Nickel-Iron nanoparticles



Amit Sharma^{a,b}, Oz Mendelsohn^{a,1}, Anuj Bisht^a, Johann Michler^b, Raj Kiran Koju^c, Yuri Mishin^{c,*}, Eugen Rabkin^{a,*}

- ^a Department of Materials Science and Engineering, Technion Israel Institute of Technology, 3200003 Haifa, Israel
- ^b Empa, Swiss Federal Laboratories for Materials Science and Technology, Laboratory for Mechanics of Materials and Nanostructures, Feuerwerkerstr. 39, Thun CH 3602 Switzerland
- ^c Department of Physics and Astronomy, MSN 3F3, George Mason University, Fairfax, VA 22030, USA

ARTICLE INFO

Article history: Received 15 June 2022 Revised 21 September 2022 Accepted 11 November 2022 Available online 12 November 2022

Keywords:
Nanoparticles
Dislocations
Order to disorder phase transformations
Precipitation strengthening
Nickel-iron alloys

ABSTRACT

It is well known that metals are strengthened by alloying additions or finely dispersed precipitates of a second phase. Here we show that alloying pristine, defect-free single crystalline nickel nanoparticles with iron results in a counter-intuitive softening due to randomly distributed solute (Fe) atoms and nano-size precipitates of the ordered Ni₃Fe or Fe-rich phases. The Ni-Fe particles with Fe concentration of 0-50 at.% were synthesized by solid-state dewetting of Ni-Fe bilayer thin films deposited on a sapphire substrate. Ni-27Fe and Ni-50Fe particles exhibited a bimodal size distribution with small (111) and large (100) oriented particles. The solid solution softening was observed in all particles. The precipitation softening was observed in (100) oriented Ni-27Fe particles with uniformly distributed ordered Ni₃Fe (L1₂) precipitates. Fe-rich precipitates were found on the surfaces and near the edges of the highly alloyed Ni-50Fe particles, leading to even greater softening. Molecular dynamic simulations of particle deformation have demonstrated that the softening effect is associated with premature dislocation nucleation at sites with a local stress concentration caused by the randomly distributed solute atoms. This work illustrates how the classical hardening mechanisms operating in bulk materials can be manipulated and even reversed in defect-free single-crystalline metal nanoparticles whose plastic deformation is controlled by dislocation nucleation.

© 2022 Acta Materialia Inc. Published by Elsevier Ltd. All rights reserved.

1. Introduction

It is well established that plastic deformation mechanisms in the metal samples of submicrometer dimensions are different from those in bulk metals [1,2]. The change in the deformation mechanisms is often discussed in terms of scarcity of dislocation sources and proximity of free surfaces where dislocations can annihilate or escape [3,4]. In contrast to bulk metals, where the motion of preexisting dislocations controls the deformation, the plasticity of pristine single crystals without preexisting dislocations is controlled by stress-induced nucleation of new dislocations [5]. The nucleation of new dislocations requires much higher stresses than for activating existing dislocation sources or moving existing dislocations through obstacles [4]. Recent examples showing different mechanical responses in small samples include the strength dependence

on the sample shape [6–9], phase transformations during deformation [10], metastable phase formation [11], and the effect of alloying [12] and surface modifications on the strength [13,14].

Fabricating defect-free metallic structures is challenging because defects naturally form during crystal growth or are introduced during the Focused Ion Beam (FIB) machining [15]. The exposure of defect-free single-crystalline samples to ion beams leads to softening. Plastic deformation becomes more homogenous without strain bursts which are "signatures" of nucleationcontrolled plasticity [16-18]. Metallic nanoparticles obtained by solid-state dewetting are typical defect-free structures displaying a high compressive strength close to the theoretical limit [17–21]. These high-strength particles could be of interest in many applications, such as additives in coatings, composites materials, polishing suspensions, and lubricants [22]. Moreover, with the elastic limit comparable to that of bulk superelastic alloys (11 %) and much higher strength, such particles are excellent candidates for spring elements and contacts in microelectromechanical systems. Pristine nano- and microparticles of face centered cubic (FCC) and body centered cubic (BCC) metals demonstrate similar deformation

^{*} Corresponding authors

E-mail addresses: ymishin@gmu.edu (Y. Mishin), erabkin@technion.ac.il (E. Rabkin).

Now at: Data Science Group, 30 Haarba'a street, Tel Aviv, Israel

behavior, with load-displacement curves displaying an elastic loading segment up to very high strains (\sim 0.2) followed by a sudden catastrophic failure. The atomistic molecular dynamic (MD) simulations helped understand the deformation mechanisms responsible for the high strengths [19,20].

Most of the previous investigations on plastic deformation of defect-free particles focused on the shape and size dependence of the strength in pure metals [4,18-21]. The size effect on the strength of single-crystalline faceted particles was discussed in terms of the stress gradient along different active slip planes determined by MD and finite element simulations. The particle shape effect on the strength was also explored [22-25], showing that rounded edges and corners can significantly reduce the stress concentration and increase the particle strength. The ultrahigh strength of Ni (34 GPa) [19] and Mo (46 GPa) [20] particles with rounded edges was explained by heterogeneous dislocation nucleation at the particle edges and homogenous nucleation in the particle interior. The experimental results were supported by MD simulations, which revealed that the edge blunting by gradual removal of high-energy atoms from the edges of low index facets eliminated the most favorable sites for heterogeneous dislocation nucleation and led to homogenous nucleation in the particle inte-

In this work, we address the question of whether the traditional strengthening strategies employed in the classical metallurgy can be utilized to further increase the strength of pristine singlecrystalline metallic particles. The classical strategies include solid solution strengthening [27], precipitation strengthening [28], the Hall-Petch (grain-size) strengthening [29], grain boundary engineering [30], and the tailoring of gradient microstructures [31,32]. Significant improvements in strength and strength-ductility tradeoff have been achieved, although the strength of bulk materials remains far below the theoretical limit. The most common approach is solid-solution strengthening, in which the solute atoms act as pinning sites to hinder or block the dislocation motion. By contrast, it was recently shown that adding solutes to defect-free nanoparticles may cause their softening rather than strengthening. This inverse effect was interpreted as the impact of solute atoms on the dislocation nucleation. In two separate studies, Zou et al. [12] and Bisht et al. [33] concluded that the softening is caused by easier dislocation nucleation at the surface. The solute atoms can facilitate the nucleation either due to the misfit coherency strain created by surface segregation in a thin film or due to solute-induced statistical variations of the local resolved shear stress in the nearsurface region in nanoparticles. At the same time, no definitive conclusion could be drawn on the effect of Au alloying on the compressive strength of pristine Ni particles [34].

Another common approach to improving the strength of bulk alloys is precipitation strengthening, in which dislocation interaction with second-phase precipitates and their elastic strain field leads to substantial hardening of the alloy. The improvement in strength depends on the type of precipitate-matrix interface and the size and distribution of the precipitates [35]. The influence of precipitates on the dislocation nucleation-controlled plasticity and plastic deformation in defect-free nanoparticles has not been explored.

Long-range chemical order usually leads to an increase in hardness and flow stress of bulk alloys, which is reflected in the term "order hardening" coined to describe the phenomenon [36]. The hardening effect increases with decreasing size of antiphase domains in the ordered structure [36,37]. Several experimental and computational studies have addressed the strength of pristine Ni₃Al nanoparticles with the ordered L1₂ structure [17,26,38,39]. However, because this alloy is fully ordered up to the melting temperature, the long-range order contribution to strength cannot be probed. To the best of our knowledge, the effect of order-disorder

phase transformations on the strength of defect-free single crystal particles under uniaxial compression has not been explored.

Here, we study the effect of Fe addition on the morphology and strength of Ni-rich Ni-Fe particles. Ni-Fe is selected as a model system for the following reasons. Ni and Fe are fully miscible, forming an FCC solid solution at temperatures above 517°C [40]. A first order order-disorder phase transformation occurs near the Ni₃Fe composition. Two-phase polycrystalline Ni₃Fe alloys with fine domains of the L12-ordered phase in a disordered matrix exhibit higher yield stress than fully ordered alloys [41]. The Ni-50Fe alloy is expected to be in a two-phase state at room temperature, yet the transformation temperature is so low (347°C) that no homogeneous precipitation of the Fe-rich phase is observed upon cooling from higher temperatures. However, heterogeneous nucleation of the Fe-rich phase might occur at the corners and edges of faceted particles, similar to the earlier observations by Amram et al. in Au-Fe particles obtained by solid state dewetting [42]. Since the dislocation nucleation also occurs at the particle corners and edges, the mechanical behavior of the particles can be significantly affected by such precipitates.

2. Experimental and modeling methods

2.1. Sample fabrication

Four different bilayer films with target chemical compositions Ni_{1-X} -Fe_X (X = 0, 20, 27, and 50 at.%) were deposited on a singlecrystalline (0002) sapphire substrate (Fig. 1a). Before the deposition, the substrate wafer was cleaned with acetone, ethanol, isopropanol, and de-ionized water. The deposition was carried out in an ultra-high vacuum chamber with a base pressure of 5.0×10^{-7} Torr at a deposition rate of \sim 0.5 Å/s. The individual Ni and Fe layer thicknesses were adjusted to achieve the desired alloy compositions while keeping the total film thickness constant at \sim 27 nm. The films were annealed in a resistive tube furnace GSL-1500X-OTF (MTI corporation) under high purity forming gas atmosphere (Ar-10% H₂). A cleaned bare sapphire substrate was placed between the sample and the quartz boat to avoid contamination during the annealing. The dewetting was carried out at the annealing temperature of 1050°C for 12 hours (Fig. 1b). The heating and cooling rate was kept low at 2°C/min to achieve complete intermixing of the layers. The film compositions in the phase diagram, the annealing temperature, and the annealing protocol are shown in Fig. 1(b,c).

2.2. Sample characterization

The morphology of the dewetted particles was characterized by high-resolution scanning electron microscopy (HRSEM, Zeiss Ultra-Plus). The high-resolution micrographs were acquired using a secondary electron detector (SE) at an acceleration voltage of 4 keV. The height and surface topography of the particles was examined by atomic force microscope (AFM; Park Systems XE-70) in a tapping mode using Si tips (NSG30; NTMDT). The height and cross-sectional area of individual particles were analysed with ImageJ and XEI software for SEM and AFM images, respectively. X-ray diffraction measurements (Rigaku Smartlab) were performed on the dewetted samples with $CuK\alpha$ radiation and parallel beam optics. The instrument was equipped with a Germanium 2 bounce monochromator to remove the $K_{\alpha 1}$ and K_{β} contributions from the source. The location-specific cross-sectional lamella preparation of the dewetted particles was carried out in an FEI Helios Nanolab G3 Dual-beam FIB. The conventional and highresolution scanning/transmission electron microscopy of the samples was performed in aberration-corrected Themis G2 300 TEM operating at 300 keV. For chemical analysis, elemental distribution

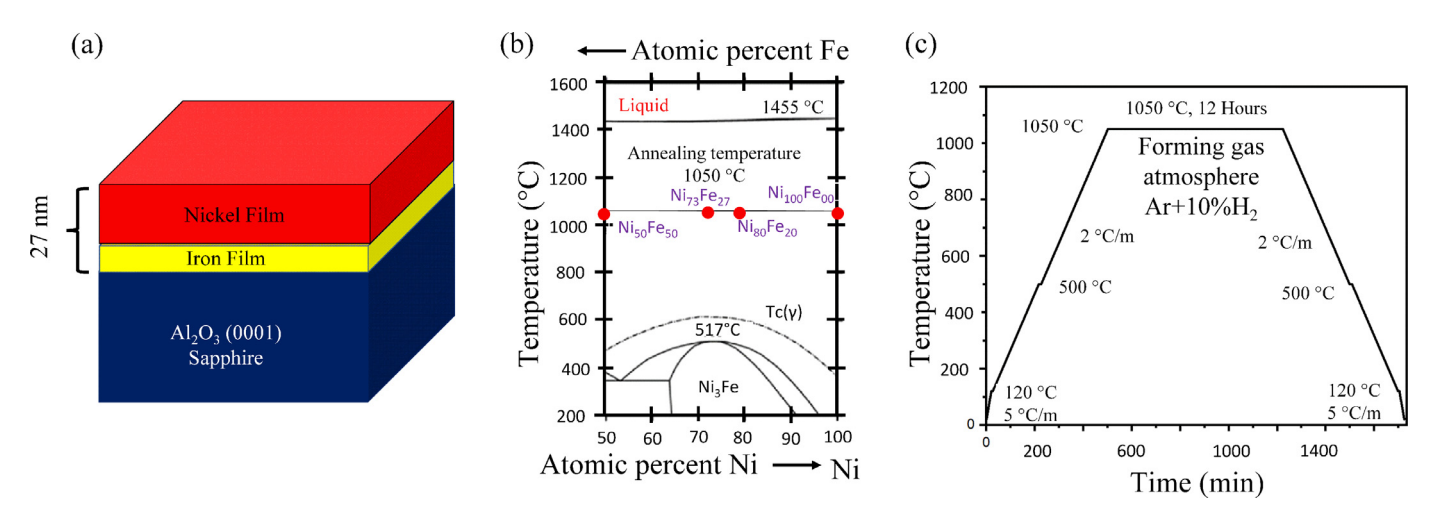


Fig. 1. Synthesis of defect-free faceted Ni-Fe particles by solid-state dewetting. (a) Schematic of the stack of two as-deposited layers. (b) Section of the binary Ni-Fe phase diagram indicating the range of compositions and annealing conditions implemented in this work. (c) Heat treatment protocol used for the dewetting of the films.

maps were recorded using energy-dispersive X-ray spectroscopy (EDS) in the scanning transmission electron microscopy (STEM) with a Super-XTM system composed of four silicon detectors. The micromechanical compression experiments were performed with an in-situ Hysitron PI85 picoindenter equipped with a 1 μ m diamond flat punch tip. The load-displacement data was acquired in a displacement-controlled mode with the displacement rate maintained at 1 nm/s. Secondary electron images with low current dose conditions were recorded before and after the compression test to ensure single particle compression at a time.

2.3. Atomistic simulations

The atomistic simulations employed the angular-dependent potential (ADP) for the Ni-Fe system [43]. ADP interatomic potentials are based on the embedded-atom method and additionally include bond-angle-dependent interatomic interactions [43]. The MD simulations employed the Large-scale Atomic/Molecular Massively Parallel Simulator (LAMMPS) package [44]. Temperature was controlled by an Anderson thermostat, and the time integration step was chosen to be 3 fs. Semi-grand canonical Monte Carlo (MC) simulations were performed to create equilibrium chemical order in Ni₃Fe particles using the Parallel Grand Canonical Monte Carlo (ParaGrandMC) code [45]. The atomic structure of the particles at the different stages of the simulations was visualized using OVITO tool [46].

Chemical ordering in the particles was characterized by a long-range order parameter X defined by two methods. In one method, X was defined by the equation

$$X = 1 - 4N_{Fo}^{Ni},\tag{1}$$

where N_{Fe}^{Ni} is the atomic fraction of the Fe atoms in the Ni sites. As a cross-check, X was also computed by a second method employing the equation

$$X = 1 - \frac{4}{3} N_{Ni}^{Fe}, \tag{2}$$

where N_{Ni}^{Fe} is the atomic fraction of the Ni atoms in the Fe sites. Both order parameters vary between 0 (disordered state) and 1 (perfect long-range order).

The order-disorder phase transformation temperature in Ni_3 Fe predicted by the ADP potential was found by calculating the equilibrium long-range order parameter as a function of temperature, T, in the interval between 700 and 900 K. The MC simulations utilized a cubic periodic block containing 13,500 atoms. After the system reached thermodynamic equilibrium, the order parameter X at

the chosen temperature was obtained by averaging over 6000 MC steps per atom. From the function X(T) obtained (see Fig. S1 in the Supplementary File), the transformation temperature was found to be about 845 K, which is in good agreement with the experimental Fe-Ni phase diagram. Accordingly, the temperatures of 900 K and 700 K were chosen for the subsequent study to represent the disordered and ordered states of the Ni_3 Fe phase.

Visualization of dislocations in the ordered L12 structure is a non-trivial task, especially for moving dislocations at finite temperatures. The most common dislocations in L1₂ structures are <110> screw superdislocations, which are dissociated into (1/2)<110> superpartials separated by an antiphase boundary (APB) on a {1 1 1} plane. In turn, each superpartial can dissociate into Shockley partials separated by a complex stacking fault (CSF). Alternatively, the superdislocation can dissociate into (1/3)<211> Kear superpartials bounding a superlattice intrinsic stacking fault (SISF). Thus, a full characterization of the dislocation cores requires the ability to visualize the APB, CSF and SISF planar faults. In this work, we developed an algorithm for detecting and visualizing planar faults in L1₂ structures by assigning a species-dependent order parameter to each atom according to the number of asymmetric bonds. This order parameter enabled us to discriminate between the different types of the planar fault and visualize them accordingly. Technical details of the parameter can be found in the Supplementary File.

Single-crystalline faceted Ni particles of an equilibrium Wulff shape were created using the surface energies of different surface orientations calculated with the ADP potential (2.005, 2.172 and 2.329 J/m^2 for the {111}, {100} and {110} surfaces, respectively). Particles of different sizes but the same Wulff shape were carved out of a large cube of perfect FCC Ni. The as-carved particles exhibited sharp facet edges that could cause unrealistically strong stress concentration in the compression tests [7,19]. Therefore, we performed the edge rounding procedure [19,33], in which atoms with the highest energy were incrementally removed from the particle surface. The particle energy was minimized by the molecular statics method after each increment of this "virtual surface etching" process. The process was repeated until the particle shape became similar to the typical shape of the experimental particles (see Fig. S2 in Supplementary File). This procedure produced a set of faceted Ni particles of different sizes with properly rounded edges.

Ni₃Fe particles were created using the pure Ni particles as templates and filling their shapes with the Ni₃Fe structure. All particles obtained were then equilibrated by long MC simulations at 900 K for pure Ni and disordered Ni₃Fe phase, and at 700 K for the ordered Ni₃Fe phase. After the MC anneals, the particles were cooled

down to room temperature (300 K) for mechanical testing. When discussing the size dependence of the particle strength, we use the initial (pre-test) particle diameter defined as the average value of the largest distance between surface atoms in the x and y directions.

The particles were deformed in compression at the temperature of 300 K by placing them between two virtual harmonic walls representing the indenter and the substrate. The position of the lower wall representing the substrate was fixed, while the upper wall representing the indenter was moved towards the particle along the *z*-axis with the velocity of 1 m/s. This process simulated the displacement-controlled conditions implemented in the experiments. The simulations implemented non-periodic "shrink wrapped" boundary conditions in which the faces of the simulation box could change to always to encompass the atoms in the three spatial dimensions. Before starting the compression, the particle was thermalized at 300 K by a 75 ps MD run.

The interaction energy between the atoms and the walls is given by

$$E = k(z - z_c)^2 \tag{3}$$

where k is a force constant, z is the difference of z-coordinates of the atom and the current wall position, and $z_{\rm C}$ is a cut-off distance beyond which the atoms no longer interact with the wall. As was shown in the previous work [19], a good quantitative agreement between MD results and the experimental microcompression tests can be achieved by adjusting the wall "softness" to account for the relatively soft layer of native Ni oxide. In this work, the simulations were performed for two types of walls: "hard" and "soft", corresponding to the effective elastic moduli of 500 GPa and 100 GPa, respectively. The elastic modulus Y is related to the force constant k and the cutoff distance $z_{\rm C}$ by the equation $Y = 2kz_{\rm C}/A$, where $A = a^2\sqrt{3}/4$ and $A = a^2/2$ are the surface areas per atom for the (111) and (100) orientations, respectively. Thus, k and $z_{\rm C}$ can be adjusted to achieve the desired hardness/softness.

The engineering strain of the particle was computed by dividing the current distance between the walls (i.e., between the indenter and the substrate) by the equilibrium distance when they were a distance z_c away from the particle surfaces. The engineering compressive stress was obtained by $\sigma = F/A_0$, where F is the total force exerted on the wall and A_0 is the initial area of the top surface in contact with the wall. The stress distribution inside the particle was represented by the virial stress tensor computed by LAMMPS.

The compressive strength of the particle was extracted from the engineering stress–strain curve as the height of the first peak. The critical resolved shear stress (CRSS) was computed by multiplying the strength σ by the Schmid factor for the symmetrically equivalent (111) planes (excluding the top and bottom planes for the (111)-oriented particles).

3. Results

3.1. X-ray diffraction and Ni-Fe diffusional intermixing

The out-of-plane θ - 2θ XRD scans for the films annealed at 1050°C for 12 h are shown in Fig. 2. The X-ray diffraction analysis indicates the presence of (111) preferred orientation in all samples irrespective of their composition. The data reveals complete intermixing of the bilayers and the formation of single-phase particles after thermal annealing. The bulk interdiffusion coefficient in the Ni–Fe system is given by the Arrhenius equation

$$D_{Fe}^{Ni} = D_0 e^{-Q/RT}, \tag{4}$$

where $D_0=3.9\times 10^{-5}~{\rm m^2/s}$ and Q=254.9 kJ/mol for the equiatomic Ni-Fe alloy [47]. Using these parameters, the average diffusion distance $\sim\!\!\sqrt{Dt}$ during the anneal is $\sim\!\!12~\mu{\rm m}$, which is well above the

initial bilayers thicknesses (27 nm). In addition, diffusion is further accelerated by twin boundaries and large-angle grain boundaries in the as-deposited layers [48]. Thus, the anneal should result in complete intermixing of the layers and single-phase XRD peaks. The systematic shift in (111) reflection towards the lower angle (2θ) with increasing Fe concentration is attributed to the solidsolution formation and increase in the d-spacing. This increase is in line with the concentration dependence of the lattice parameter of bulk Ni-Fe alloys (Fig. 2b). The XRD spectra of Ni-27Fe and Ni-50Fe samples display additional peaks from (200) oriented particles. The second-order (400) reflection shown in Fig. 2(c) indicates the presence of a doublet instead of a single reflection. The overlapping peaks could result from either tetragonal distortion in the particles to maintain the epitaxial relationship with the substrate or from the presence of ordered precipitates in the particles. Note that no doublet or overlapping peaks are observed in second-order (222) peaks (Fig. 2(d)).

3.2. Effect of composition on particles morphology

The HRSEM micrographs of the nanoparticles of different compositions formed after complete dewetting are shown in Fig. 3(a-d). The Ni and Ni-20Fe particles exhibit a truncated octahedron morphology with the upper hexagonal facet parallel to the substrate. This morphology is typical for FCC metallic particles with (111) out-of-plane orientation (Fig. 3(e,f)). Since these particles were formed by a long anneal at a high homologous temperature (0.77 $T_{\rm M}$, where $T_{\rm M}$ is the melting point of Ni), they are single-crystalline without any signs of high-angle grain boundaries or twin boundaries.

The Ni-27Fe and Ni-50Fe particles show a bimodal size distribution with (111) oriented small particles and (100) oriented large particles (Fig. 3(c,d)). The HRSEM images in Fig. 3(g,h) show that most (111) oriented small particles have reached equilibrium crystal shape (ECS) with a similar arrangement of facets, irrespective of the composition. However, most (100) oriented large particles remain elongated parallel to the substrate and far from their ECS. The geometrical parameters of (111) particles for different compositions are shown in Fig. S3 of Supplementary Material. The large scatter in data indicates that most of the particles formed after solid-state dewetting are far from their ECS. The particles with such a low aspect ratio resemble small patches of thin films and are not suitable for micromechanical testing. Therefore, several locations were scanned with AFM to select the particles having an aspect ratio (height/diameter) suitable for nanomechanical testing. Here, for reference, we are using the results of Meltzman et al. for the ECS of Ni particles [50], according to which the aspect ratio for most of the equilibrated Ni particles on (0002) sapphire substrate ranges from 0.7 to 1.0.

While the morphology and facet arrangement in Ni-27Fe and Ni-50Fe particles are similar (Fig. 4), the Ni-50Fe particles display signs of precipitation. The small precipitates are uniformly distributed on the surfaces and edges of the particles, irrespective of their shape and orientation (indicated by arrowheads in Fig. 4(b,d)). The arrangement of the facets remains unaffected by these precipitates. The high magnification HRSEM image of the faceted (111) particle is compared with the simulated model of a fully faceted particle (Fig. 4(f)) obtained with WinWULFF freeware [51]. The relative energies of the different surfaces were adjusted to achieve the best agreement with the experimentally observed particle morphology. The following facets were identified: {111}, {010}, {120}, {011} and small {240} facets, with the Ni-Fe (111) || Al₂O₃ (0002) orientation relationship to the substrate as confirmed by XRD (Fig. 2). The facet analysis of (100) oriented particles shown in Fig. 4(e) indicates that most of the fundamental low index facets are still present in the particles. However, {131} facets are absent,

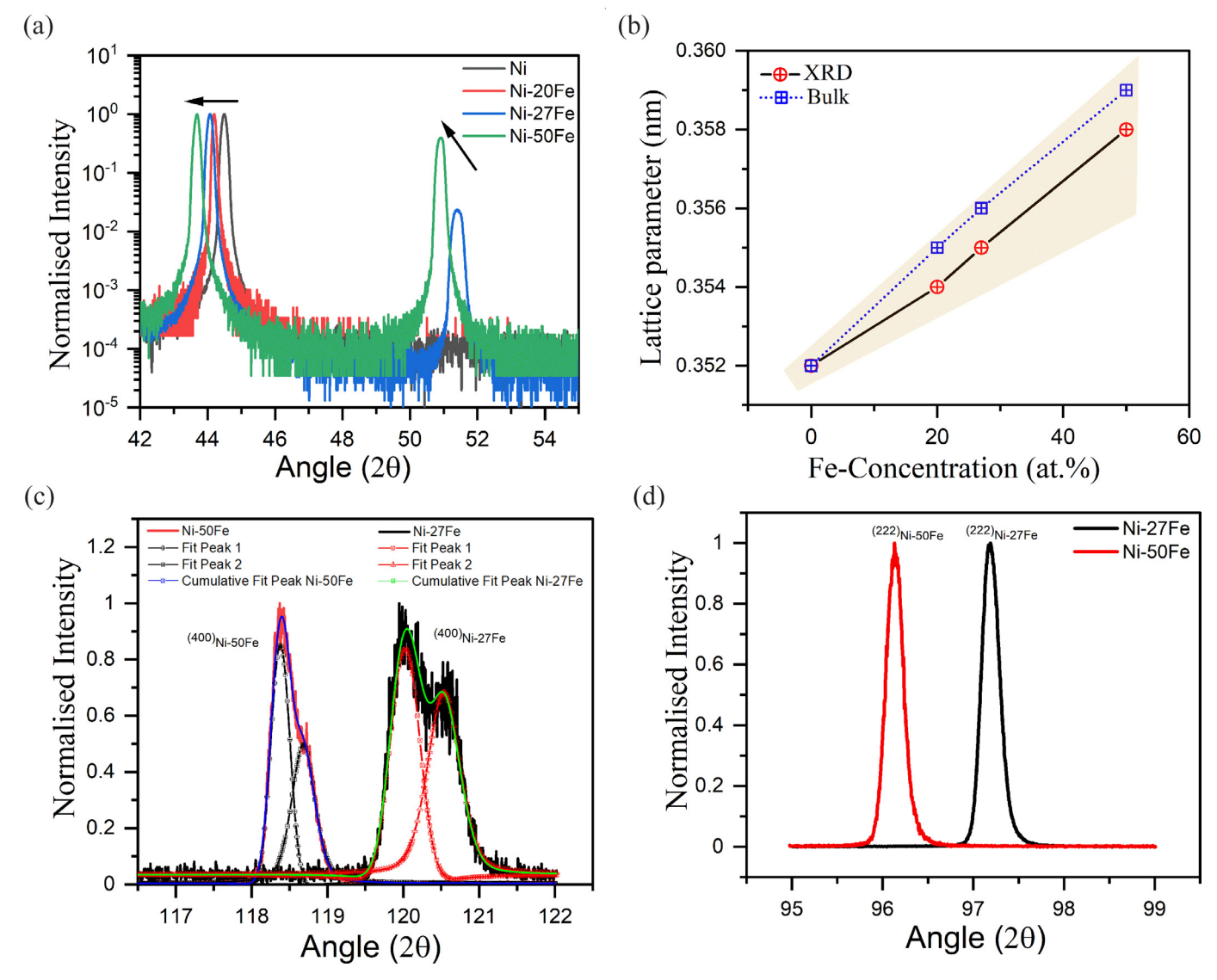


Fig. 2. XRD scans of particles formed after annealing for 12 h at 1050° C. (a) Out-of-plane X-ray data showing preferred (111) orientation in Ni and Ni-20Fe particles. The Ni-27Fe and Ni-50Fe samples show (111) and (100) orientations. Gradual shift of the (111) reflection towards lower 2θ angles with increasing Fe concentration confirms the solid solution formation. (b) Lattice parameters calculated from XRD data compared with lattice parameters from bulk samples. (c) HR-XRD data showing the peak splitting (initial indication of phase separation) of (400) reflections from Ni-27Fe and Ni-50Fe particles and deconvoluted profiles fitted over the measured profiles using the Fityk Peak analysis program [49]. (d) HR-XRD data showing (222) reflections with no peak splitting from Ni-27Fe and Ni-50Fe particles.

and the relative surface area of the {120} and {110} facets is different from that in the (111) particles.

The structural analysis of the ensemble of particles by XRD measurements is further confirmed by TEM analysis on TEM lamella prepared through the center and aligned with symmetry planes of an individual particle. The conventional bright-field (BF) image and selected area electron diffraction pattern (SAED) for a (100) oriented Ni-27Fe particle are shown in Fig. 5a and b, respectively. The BF image displays {111}, {200}, {110} and {120} facets, in agreement with in the model shown in Fig. 4e. The SAED pattern displays fundamental reflections and superlattice reflections corresponding to the [001] zone axis pattern (Fig. 5b). The superlattice reflections indicate the presence of long-range L12 order in the particle. The dark field image collected from (010) reflection shows uniformly distributed fine precipitates of ~5 nm in size (indicated by arrows in Fig. 5c). A similar analysis has been performed for (111) oriented Ni-27Fe particles prepared along the [011] zone axis. The orientations analysis reveals the presence of {111}, {110}, {100}, and {112} facets (Fig. 5f). The SAED pattern obtained along the [011] zone axis exhibits sharp diffraction spots typical for single-crystalline particles without superlattice reflections (Fig. 5g).

The elemental maps (Fig. 5(d,h) confirm the chemical homogeneity of both particles with no signs of segregation on the surface or the particle-substrate interface. The EDS line profile shows that the average chemical composition of particles is Ni-Fe27 (at.%) irrespective of the orientation (Fig. 5e,i). The average Fe concentration in the particles is close to the initial stack's composition before the heat treatment.

A similar analysis has been performed for Ni-50Fe particles prepared in different zone axis conditions. The BF micrograph and SAED pattern for a (100) oriented Ni-50Fe particle are shown in Fig. 6(a,b). The BF micrograph displays the presence of sharp facets and small precipitates on the (111) facets. The SAED pattern exhibit sharp diffraction spots typically observed in single-crystalline particles. Although the HRXRD analysis shows peak splitting in the (400) reflection similar to the Ni-27Fe particle, no superlattice reflections are observed in this case. The S/TEM EDS elemental map shown in Fig. 6(d) indicates that the precipitates are

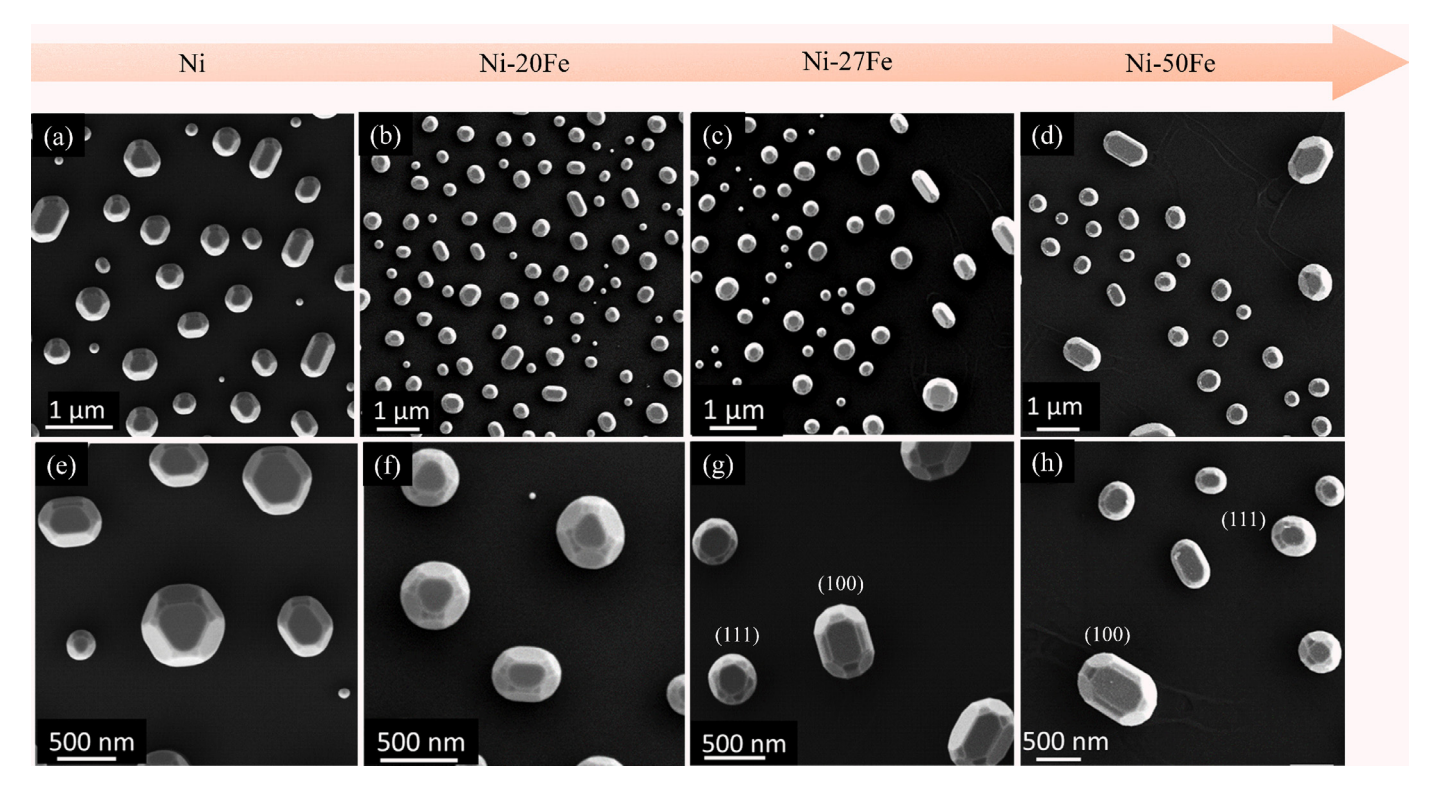


Fig. 3. FE-SEM micrographs of the defect-free single-crystalline (a) Ni, (b) Ni-20Fe, (c) Ni-27Fe, and (d) Ni-50Fe particles obtained by dewetting of bilayer thin films. The Fe concentration increases from left to right. Higher magnification images show distinct facets and morphology of (a) Ni, (b) Ni-20Fe, (c) Ni-27Fe, and Ni-50Fe particles. The small (111) and large (100) particles can be seen in Ni-27 (g) and Ni-50Fe (h) samples.

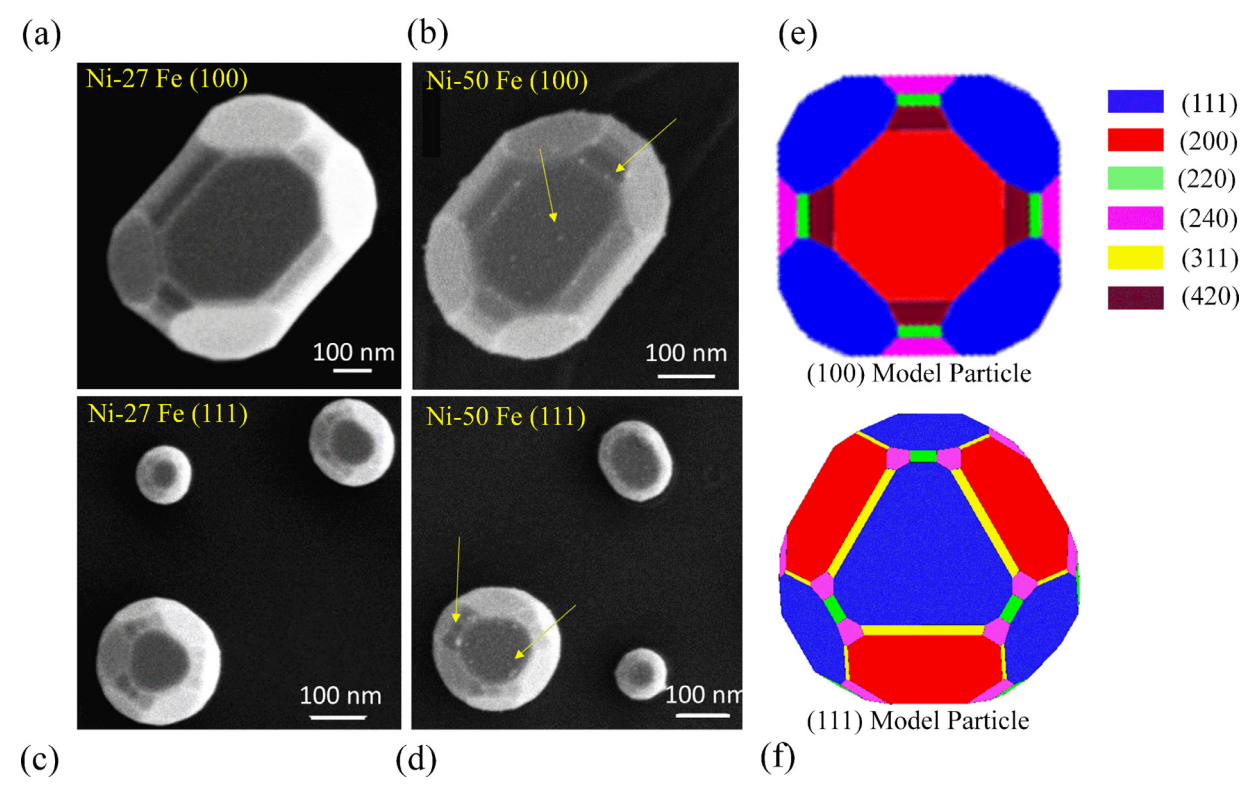


Fig. 4. High-magnification SE image showing (a,b) Ni-27Fe and (c,d) Ni-50Fe particles with (111) and (100) orientations. The facet arrangement is the same for both compositions. Ni-50Fe particles display fine precipitates on the surfaces and edges (indicated by arrows). (e,f) The model ECS of (100) and (111) particles generated by WinWulff software.

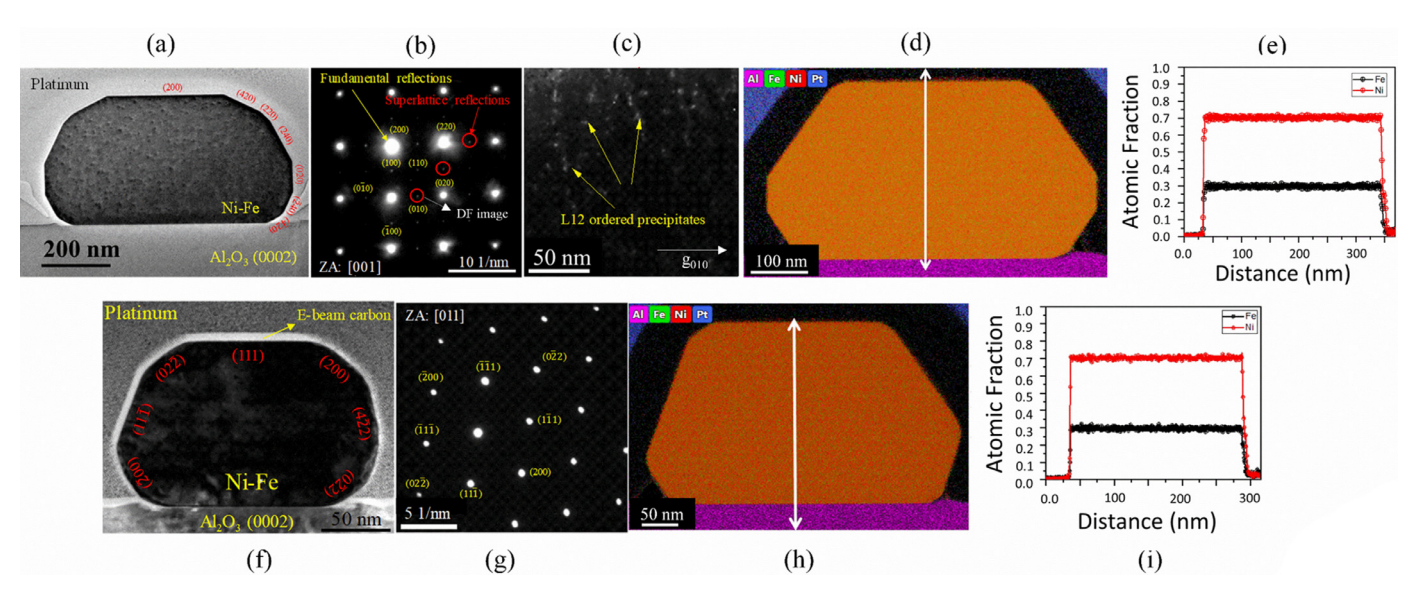


Fig. 5. S/TEM characterization of Ni-27Fe nanoparticles fabricated by solid-state dewetting. (a) Bright-field (BF) image of the (100) oriented particle along the [001] imaging direction. (b) SAED pattern containing fundamental and superlattice reflections. (c) Dark-field image from the superlattice reflection showing L1₂ precipitates distributed uniformly within the particle. (d) S/TEM EDS elemental map showing the protective Pt layer, Ni-Fe particle, and sapphire substrate (the vertical arrow indicates the location for EDS line scan for quantitative analysis). (e) Concentration profile along the line. (f,g) BF image of Ni-27Fe (111) oriented particle seen along [011] direction and SAED pattern showing only fundamental reflections. (h, i) S/TEM elemental distribution maps and concentration line profiles along the line indicated in the elemental map.

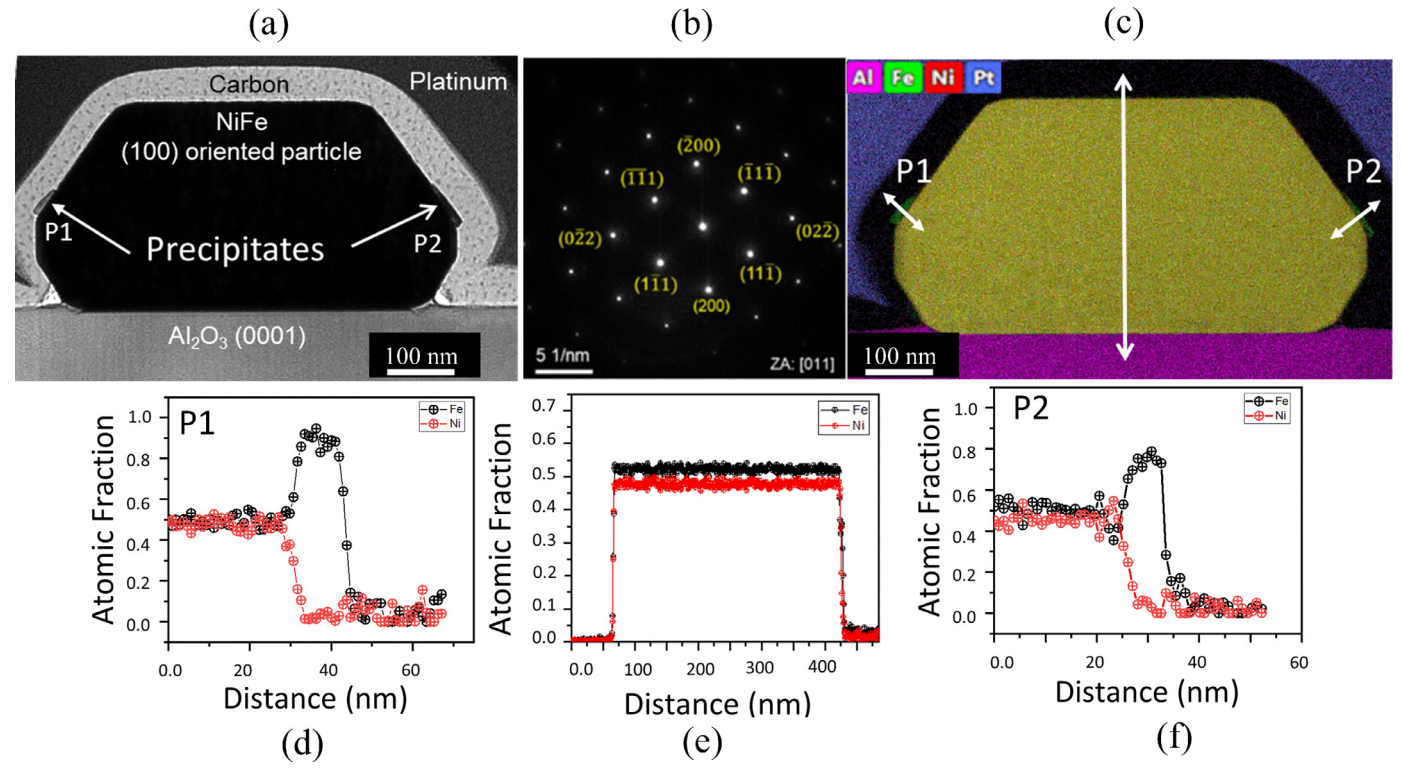


Fig. 6. S/TEM characterization of Ni-50Fe nanoparticles produced by solid-state dewetting. (a) BF image of (100) particle showing the precipitates P1 and P2 on the facets. (b) SAED pattern along [011] zone axis. (c) S/TEM EDS elemental maps showing Fe-rich precipitates and arrows for elemental line scans. (d,e,f) Concentration line profiles from the particle and precipitates P1 and P2.

iron-rich, which is further confirmed by acquiring EDS line scans across the precipitates (Fig. 6(e,f)). The particle interior exhibits a uniform composition with no signs of elemental segregation. The EDS line scan across the particles shows the Ni/Fe ratio of 47/53, which is slightly higher in Fe content than the composition of the original stack (Ni/Fe: 50/50). The slight surplus of Fe could be an artifact caused by a weak background signal from the sample holder. A measurable concentration gradient is observed in

the vicinity of the P2 precipitate. The TEM BF image, SAED pattern, and S/TEM chemical analysis of (111) oriented Ni-50Fe particle is shown in Supplementary Fig. S4. The BF image of this particle displays a similar facets arrangement as observed in the (111) oriented Ni-27Fe particle. The SAED pattern exhibits sharp diffraction spots indexed with [112] zone axis pattern. The S/TEM EDS maps and composition line profile indicate a homogenous Ni/Fe ratio of 46/54. Again, the composition is slightly Fe rich and can

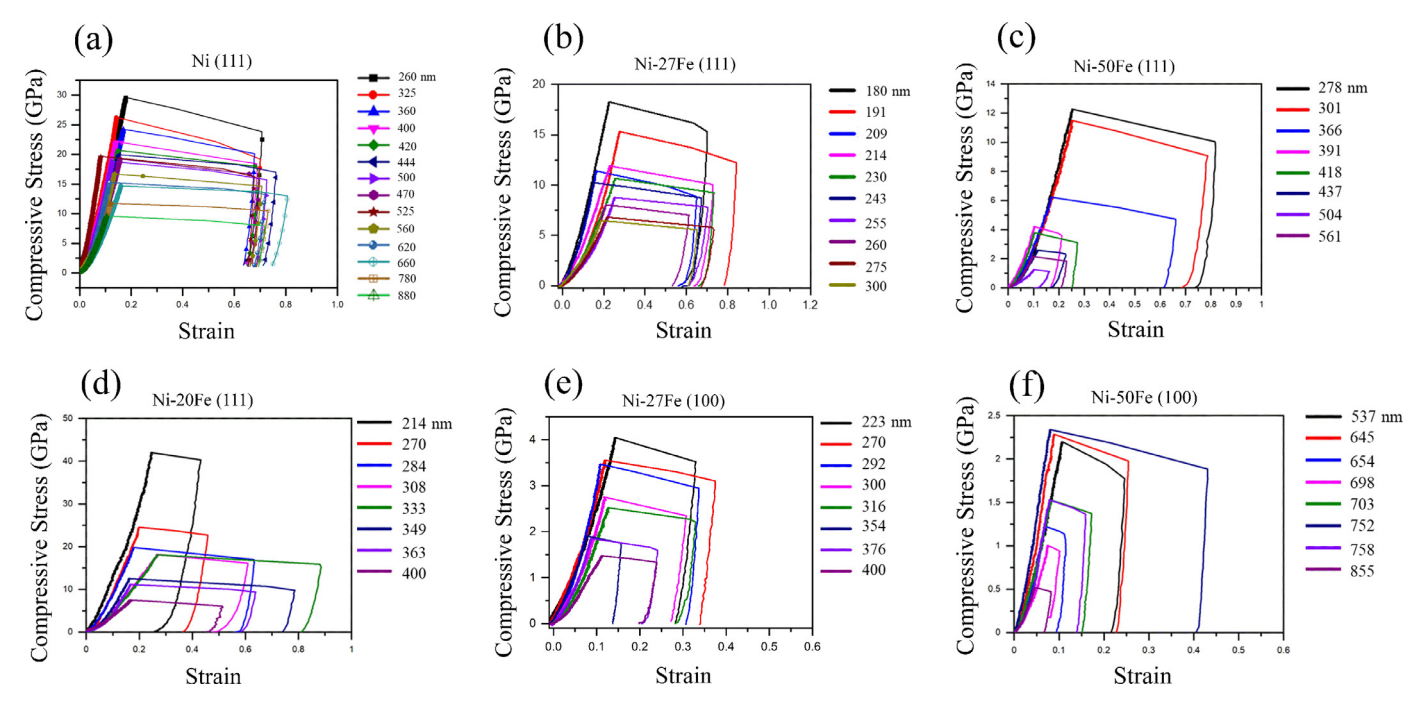


Fig. 7. Nanomechanical testing of Ni and Ni-Fe particles. Engineering stress-strain curves for (a) Ni, (b) Ni-27Fe, (c) Ni-50Fe, and (d) Ni-20Fe (111) oriented particles. (e-f) Engineering stress-strain curves for Ni-27-Fe and Ni-50Fe particles with (100) orientation. All particles show large elastic deformation followed by catastrophic failure typical for dislocation nucleation controlled plasticity.

be explained by a weak background contribution from the sample holder.

4. In-situ micromechanical compression behavior

The compression strength of the particles was measured by *insitu* micro-compression experiments in SEM. For a better comparison, only particles close to their equilibrium shape were selected for testing. The load-displacement curves shown in supplementary Fig. S5 display a purely elastic deformation up to large displacements in the range of 10-25% of the original particle height. The onset of plastic deformation can be seen as an abrupt strain burst due to a catastrophic failure, which is typical for nucleation-controlled plasticity in single-crystalline metallic particles. Note that the amplitude of displacement burst in (100) oriented particles is consistently smaller than in (111) oriented particles of the same composition and similar size. In all cases, however, the particle collapsed into pancake-like flat disks.

The load-displacement data were converted into engineering stress-strain curves to compare the strength of particles of different sizes, see Fig. 7(a-f). The engineering stress is determined by dividing the load by the top facet area in contact with the punch. The engineering strain is obtained by dividing the displacement of the indenter by the initial particle heights. It should be noted that, because of the indenter compliance and elastic deformation of the substrate, the actual strain of the particle is generally lower than the calculated engineering strain. The stress-strain curves obtained show a clear scaling effect, with smaller particles being stronger than the larger for all chemical compositions and orientations. The particle's compressive strength σ is defined as the value of the engineering stress at the onset of the catastrophic failure (strain burst).

Fig. 8 displays the compressive strength as a function of particle's effective diameter (defined as the square root of projected area) for different chemical compositions. To compare the strengths of (111) and (100) oriented particles, the σ values were converted to the CRSS τ for the {111}(110) slip system and are

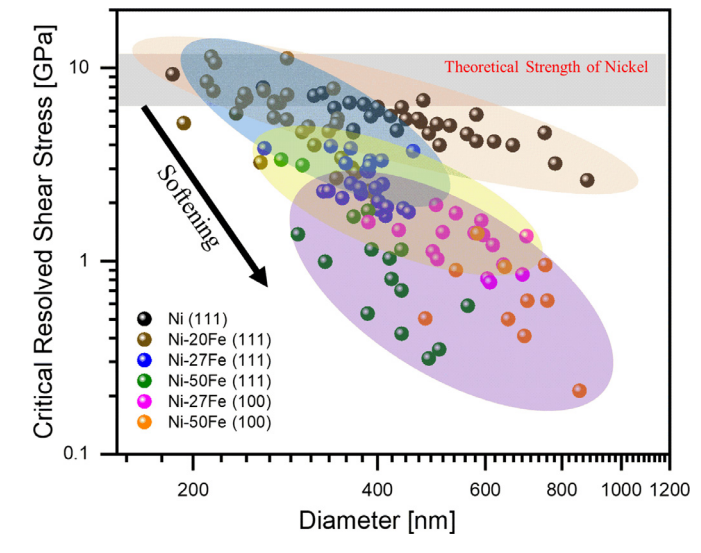


Fig. 8. A summary plot of the CRSS as a function of particle's diameter for different chemical compositions. Note the softening trend with increasing Fe concentration. The results are compared with the lower and upper bounds of theoretical strength of Ni obtained by first-principles calculations [53] and the Frenkel model [52] for the {111}<112> slip and {111}<110> slips, respectively (gray zone).

plotted as a function on particle diameter in Fig .8. The size dependence of the strength was fitted with the inverse power law $\sigma = Ad^{-n}$ (A is a constant). The size exponents n for Ni, Ni-20Fe, Ni-27Fe and Ni-50Fe (in the latter two cases for both particle orientations together) were found to be 0.7 ± 0.07 , 1.0 ± 0.2 , 1.1 ± 0.1 and 1.1 ± 0.3 , respectively (Fig. S6).

The maximum CRSS observed in the smallest particles (diameter < 300 nm) is around 10 GPa, which is very close to the theoretical shear strength of Ni predicted by Frenkel [52] and by first principles calculations [53] for {111}<110> full dislocations and {111}<112> partial dislocations (indicated by the shaded gray

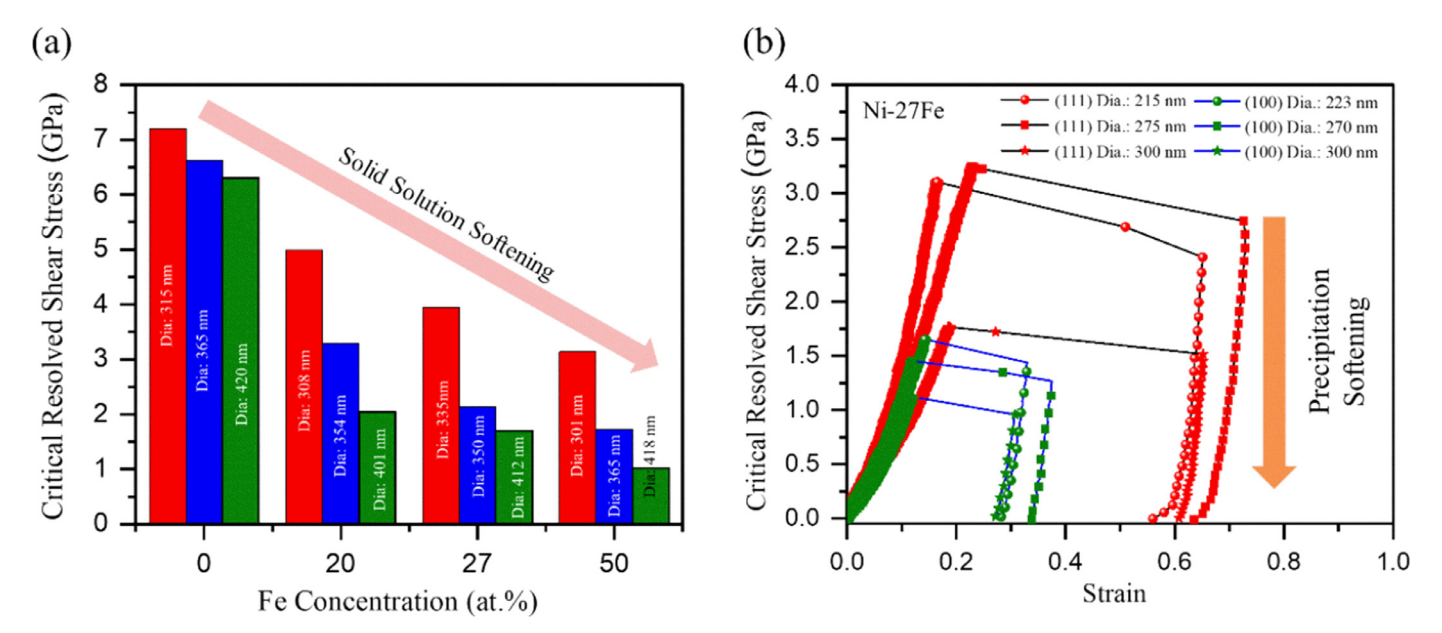


Fig. 9. Demonstration of the solid solution and precipitation softening effects. (a) CRSS versus Fe concentration for groups of particles of comparable size selected from the summary plot in Fig. 8. A monotonous softening trend with the alloying is observed irrespective of the particle size. (b) Resolved shear stress versus strain for Ni-27Fe particles for three pairs of particles with the (111) and (100) orientations and similar diameters. The partially ordered (100) particles exhibit the precipitation softening effect

region in Fig. 8). The trend for the particle softening with Fe addition is apparent and agrees with the recently observed solid solution softening in Ni-Co particles [33]. Moreover, some indications of solid solution softening were found in Ni-Au particles produced by solid state dewetting, although no definitive conclusion could be drawn because of high scatter of the measured strength values [34]. The solid solution softening effect is further illustrated in Fig. 9a by comparing the CRSS values for different Fe concentrations and sizes (Fig. 9a).

One of our goals was to evaluate the long-range ordering effect on the particle strength. A direct comparison of the strength of disordered and partially ordered Ni-27 particles is difficult because there is little size overlap between the two particle populations. The (100) Ni-27Fe particles with ordered L1₂ precipitates are, on average, significantly larger than the disordered (111) particles. Still, we picked up three (100) oriented particles for which the (111) oriented counterparts of comparable size could be found. A comparison of the resolved shear stress vs. strain curves is shown in Fig. 9b. The significantly smaller CRSS in partially ordered particles lends credibility to the hypothesis that the small ordered precipitates cause particle weakening.

The weakening of the particles of both (111) and (100) orientations is especially strong for the Ni-50Fe composition. This strong weakening can be attributed to the combined effect of solid solution and precipitate softening. Unfortunately, the size overlap between the (100) and (111) oriented particles, with the (100) particles being larger, was insufficient for drawing meaningful conclusions about the orientation effect on the particle strength.

5. Simulated compression behavior

Fig. 10 summarizes the simulation results for 268 Ni and Ni_3 Fe nanoparticles tested in this work. The dataset includes the particles with four different sizes tested with hard and soft walls representing the indenter and the substrate. The common trend found across the entire dataset is the size dependence of the strength, with smaller particles being stronger than larger ones. This trend is consistent with the available experimental literature on the compression of pristine single-crystalline faceted particles

[4,19,20,26,33,34] and the experimental results of the present work (cf. Fig. 8).

During the compression, all particles first exhibited elastic deformation up to a few percent of strain followed by an abrupt drop of stress caused by dislocation nucleation at one of the surfaces contacting the walls. Typical stress-strain curves are shown in Fig. 11 for 30 nm particles compressed by a hard indenter. The first stress drop is followed by a series of secondary peaks, which for the (111) surface orientation have a significantly larger amplitude than for the (100) orientation. Furthermore, the first-peak stress is systematically higher for the (111) orientation than for the (100) orientation across all particles tested. The difference can be largely attributed to the different Schmid factors of the two orientations: the respective CRSS values are similar within the scatter of the data points (Fig. 10).

It is important to note that the strength of the ordered Ni₃Fe particles is consistently higher than that of disordered particles of the same orientation and size. This result is consistent with the empirical "order hardening" trend in bulk materials [36]. Fig. 11 shows that when tested with hard walls, the Ni and ordered Ni₃Fe particles exhibit a comparable CRSS, whereas the disordered Ni₃Fe particles are significantly weaker. When tested with soft walls, the (111) oriented Ni particles are somewhat stronger than the ordered Ni₃Fe particles, while for the (100) orientations, the respective CRSS values are similar. But even with soft walls, the disordered Ni₃Fe particles are the weakest of all three groups. This finding provides another example of the solid solution weakening effect in nucleation-controlled plasticity [33]. At the same time, the simulations reveal that the solute weakening rule is not followed when the alloying creates a chemically ordered phase. As already mentioned, the Ni₃Fe alloy particles with long-range order are nearly as strong as the pure Ni particles. This finding is at variance with our experimental results (see Figs 8 and 9). The reason for this apparent contradiction will be explained in the next sec-

Numerous MD snapshots were examined to understand the dislocation nucleation mechanisms. Such mechanisms were qualitatively similar in Ni and the disordered Ni₃Fe particles. In (111)-oriented particles, the first surface nucleation of a leading Shockley

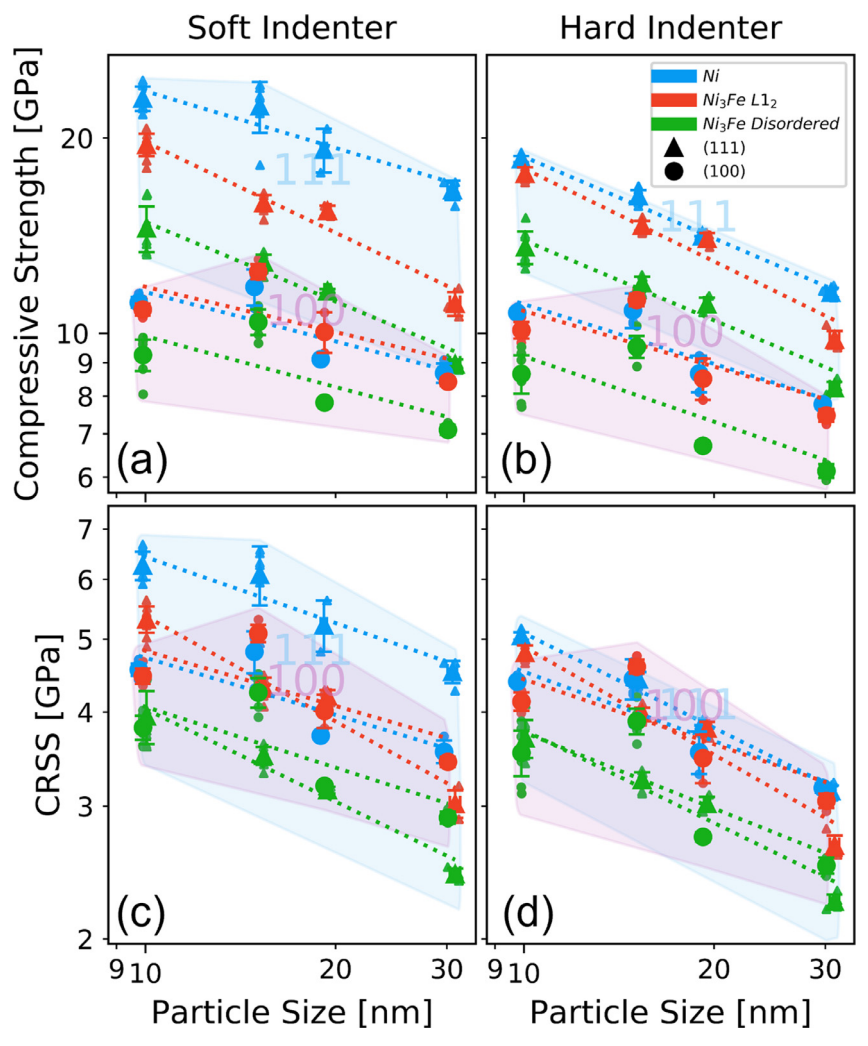


Fig. 10. Summary of simulated compression test results. (a,b) compressive strength; (c,d) CRSS. The particles were tested by (a,c) soft walls and (b,d) hard walls representing the indenter and the substrate. Note the logarithmic scales of both axes. The dotted lines are power-law fits to the data. Small symbols represent individual tests, large symbols are the respective averages.

partial dislocation was immediately followed by the nucleation of a trailing one, injecting a full dislocation into the particle interior (see Fig. S7a in Supplementary File). In Ni particles, this nucleation event was immediately followed by multiple nucleations of additional dislocations, causing a dislocation avalanche and a significant stress drop. In disordered Ni₃Fe particles, the formation of the first full dislocation was well separated in time from the subsequent nucleation events. Also, the dislocations were often pinned at some points by forming a short Lomer-Cottrell dislocation segment (see Fig. S8 and Supplementary Movie M1). Such segments could but were not observed to create an active Frank-Read source. In (100)-oriented particles, the leading partial propagated a significant distance into the particle before a trailing one nucleated, leaving behind an extended stacking fault (SF) (Fig. S7b).

In ordered Ni₃Fe particles, the dislocation nucleation mechanism was different (Fig. S9 of Supplementary File). Similar to the disordered Ni₃Fe particles, the nucleation of the leading partial was swiftly followed by the nucleation of a trailing one separated from the leading by a CSF (which can be viewed as a superposition of a stacking fault and an APB). The trailing partial left behind an APB that remained attached to the surface. The formation of SISF faults was also observed at large strains when three Shockley partials on three different glide planes reacted with an APB. The dislo-

cation dynamics of the dislocation core evolutions can be observed in the Supplementary Movie M2.

6. Discussion

Single-crystalline particles fabricated by solid state dewetting usually inherit the texture of the thin film they formed from [54]. Since the thin films of FCC metals deposited on the basal plane of sapphire exhibit a strong <111> texture, the resulting particles inherit (111) orientation [6,48,50]. In the present work, all particles of pure Ni and Ni-20Fe alloys exhibited (111) orientations, while the Ni-27Fe and Ni-50Fe particles exhibited mixed (111) and (100) orientations. In a separate study, we demonstrated that this is related to abnormal growth of (100) grains in the deposited bilayers during the anneal [55]. The dewetting of such grains sets on later than in <111> textured patched of the film and proceeds at a slower pace, resulting in larger (100) particles.

The ECS of Ni particles on sapphire has been determined by Meltzman et al. employing particles cross-sectioning in FIB [50]. In the present work, we employed the AFM-based method of Müller and Spolenak to determine the ECS of single-crystalline particles on the substrate [56], enabling larger statistics and identification of particles that reached the true thermodynamic equilibrium [57].

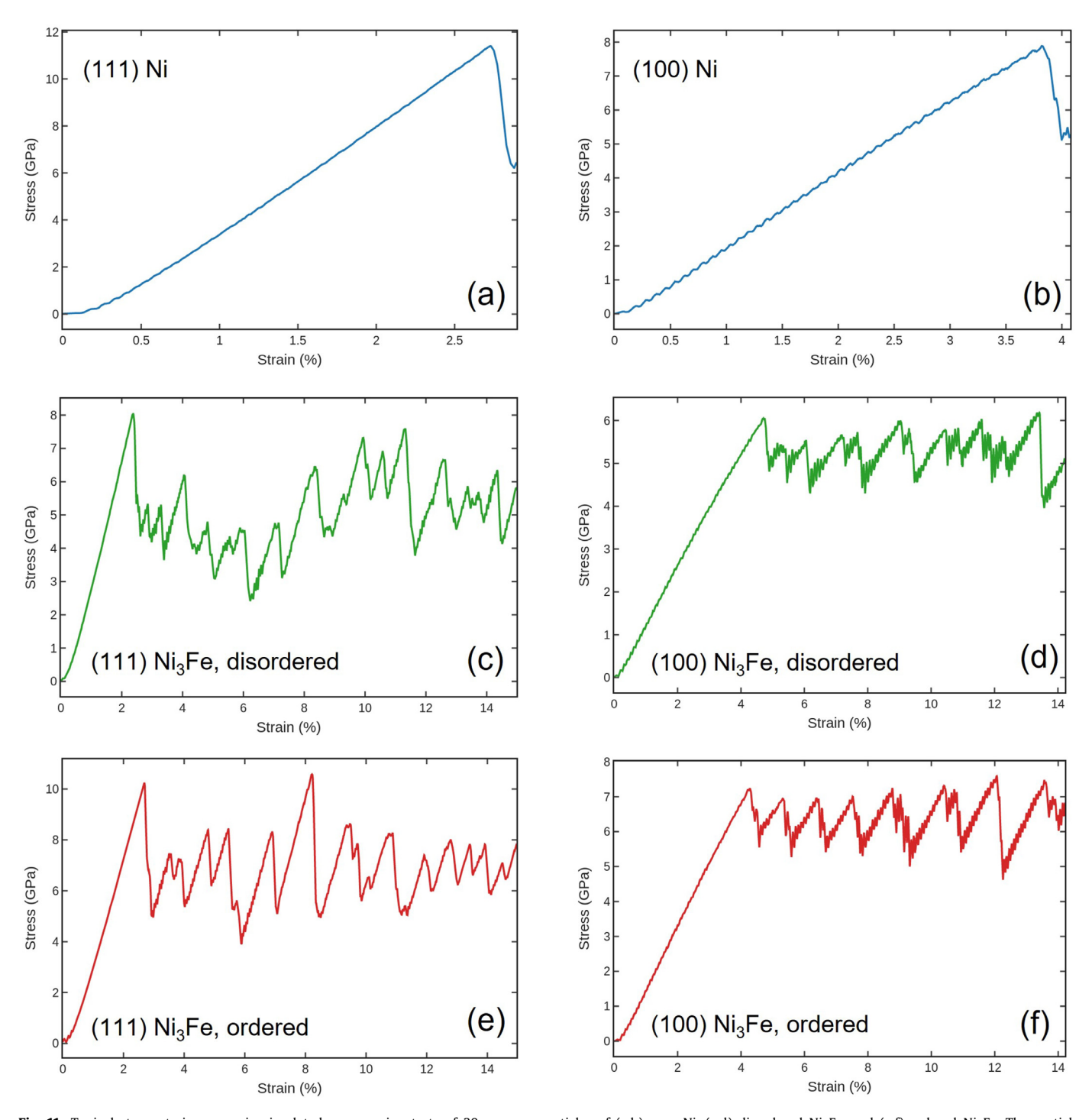


Fig. 11. Typical stress-strain curves in simulated compression tests of 30 nm nanoparticles of (a,b) pure Ni, (c,d) disordered Ni₃Fe, and (e,f) ordered Ni₃Fe. The particle orientations are (a,c,e) (111) and (b,d,f) (100). The particles were compressed by hard walls.

This method is based on finding an upper bounding line in a large dataset of particle heights and diameters. The method utilizes the fact that ECSs are self-similar and, hence, the height of truly equilibrated particles should scale linearly with their diameter. The results demonstrate that the ECSs of the Ni-20Fe and Ni-27Fe particles are similar to the ECS of Ni particles determined by Meltzman et al. [50]. This, in turn, means that in the Fe concentration range studied here, the surface energy anisotropy is only a weak function of composition. This is understandable since the surface energies of Ni and Fe are very close (about 2.4 J/m² [58]).

The abnormal grain growth in the Ni-27Fe and Ni-50Fe films prior to dewetting resulted in the formation of (100)-oriented particles at the late stages of dewetting. These particles were on average larger than the respective (111)-oriented particles. We also observed characteristic shoulders in the (400) XRD peaks (see Fig. 2c), indicating some form of phase separation in these particles. The SAED patterns and dark-field TEM images of the (100) oriented Ni-27Fe particles revealed the presence of small (about 5 nm) highly dispersed precipitates of an ordered L1₂ phase. These precipitates formed during slow cooling of the dewetted samples

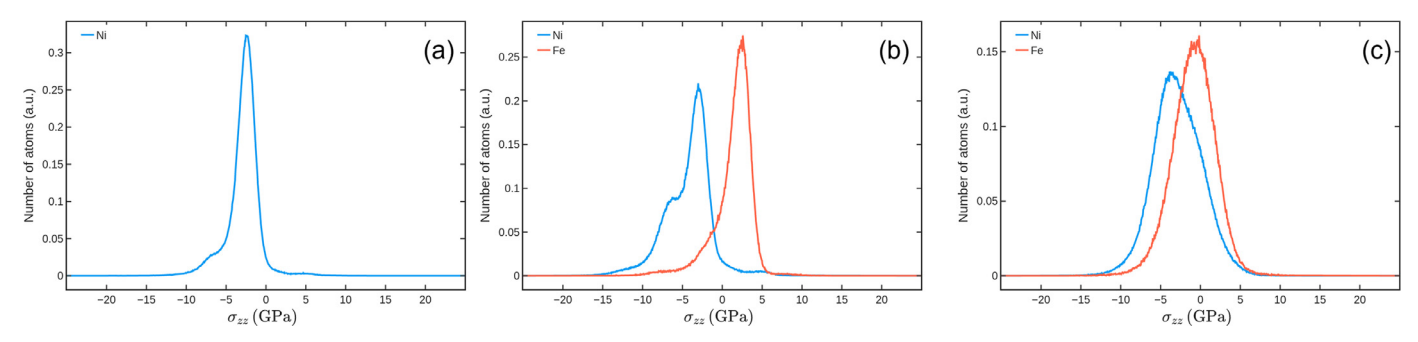


Fig. 12. Distribution functions of the atomic stress tensor component in the compression direction in the particles of (a) Ni, (b) ordered Ni₃Fe, and (c) disordered Ni₃Fe at the onset of first dislocation nucleation. The compression is performed in [100] direction with a soft punch.

when the temperature decreased below the critical temperature of the A1-L1₂ order-disorder transformation (517°C, see Fig. 1). With the Arrhenius interdiffusion parameters of $D_0 = 2.9 \times 10^{-4} \text{ m}^2/\text{s}$ and Q=273.7 kJ/mol for the Ni-30 at.%Fe alloy, the characteristic diffusion distance during dwell of 10 min at the temperature of 517°C is about 0.4 nm, comparable to the interatomic distance in the Ni-Fe alloy [47]. Since establishing long-range order requires only minor atom diffusive movements (the atoms only need to rearrange their positions on the length scale of a unit cell), this estimate suggests that slow cooling is capable of establishing some degree of longrange order in the Fe-27Ni particles. The situation is different for Ni-50Fe particles, where both the precipitation of Fe and the formation of the metastable ordered L1₀ phase occur below 350°C. At this temperature and during 10 min, the average diffusion distance is significantly lower than the interatomic distance in the Ni-50Fe alloy.

These estimates raise the question about the mechanism of the observed precipitation of Fe (see Fig. 6) and the characteristic (400) XRD peak shoulder (Fig. 2c) in the (100)-oriented Ni-50Fe particles. We note that the L10 phase has only been observed in Fe-Ni meteorites (where the typical cooling rate is a few °C per million years) or in heavily irradiated alloys with increased atomic mobility [59]. However, limited precipitation of the Fe-rich BCC phase on the particle surface cannot be ruled out because surface diffusion at low homological temperatures is by 5-7 orders of magnitude faster than bulk diffusion. The amount of Fe in the upper surface layer is insufficient to cause the amount of Fe precipitates visible in SEM and TEM (Figs 4d and 6, respectively). However, a concurrent surface diffusion-controlled change of the particle shape and precipitation of the Fe-rich phase presents a plausible scenario according to which the moving facets supply Fe atoms to the precipitates. Amram et al. proposed a kinetic model of such a surface precipitation process, concluding that the precipitate growth rate is controlled by a combination of surface self-diffusion and diffusion along the particle-precipitate interface, which are much faster than bulk self-diffusion [42]. Moreover, the precipitation may provide an additional chemical driving force for the particle shape evolution towards the ECS [60]. This scenario also explains why the Fe-rich precipitates are only observed on the surface of the particles and not in the particle interior.

While we did not observe any signs of long-range chemical order in the cross-sectional TEM studies of the Ni-50Fe particles, the characteristic shoulder in the (400) XRD peak strongly suggests that an ordered phase is present in an appreciable amount. Firstly, it may be present only in some but not all particles. That TEM did not reveal any ordered phase in one particle does not negate its presence in the others. Secondly, a partially ordered phase may be present in thin near-surface layers where precipitation of the Fe-rich phase also occurred. Thirdly, the particle-substrate interface may be an additional factor promoting local long-range order at the interface. Indeed, the ordered L10 phase is an alter-

nating sequence of (200) Ni and Fe layers. The energy of the Fesapphire interface (1.3 ± 0.1 J/m² [61]) is significantly lower than that of the Ni-sapphire interface (2.16 ± 0.2 J/m² [62]). Thus, the particle-substrate interface can promote the formation of L10 ordering in (100) oriented particles with Fe-termination at the interface. As a result, a thin near-interface layer of the L10 phase can be stable at the interface at temperatures above the critical point of the A1-L10 ordering. This is known as the prewetting phenomenon and has been reported in several alloys undergoing order-disorder transformation [63–64].

In our microcompression tests, most of the particles deformed with a single large displacement burst (see Fig. 7), indicating their nearly defect-free nature. Increasing the Fe content in disordered (111) oriented particles causes a remarkable weakening (except for the three smallest Ni-20Fe particles exhibiting somewhat higher strength than the Ni particles of comparable size), see Fig. 8. This is consistent with the findings by Bisht et al., who observed similar solid solution weakening in the particles of Ni-based Ni-Co alloys [33]. In that work, the solid solution weakening was discussed in terms of the broader Maximum Resolved Atomic Stress (MRAS) distribution in MD simulations of alloy particles compared to Ni particles. Because of the wider distribution, the critical dislocation nucleation stress at the particle edges was achieved at lower average stress in the alloy particles, making them weaker. The MD simulations performed in the present work demonstrate a similar trend. We also found that the axial component of the atomic stress tensor, σ_{zz} , is another good indicator of stress distribution in the particles. The distribution functions of σ_{zz} at the onset of the first dislocation nucleation event are shown in Fig. 12. In Ni particles, the distribution develops a shoulder at high compressive stresses (Fig. 12a), caused by stress concentration near the particle edges and corners where the dislocations nucleate. By contrast, the stress distribution in disordered Ni₃Fe particles is broader and nearly symmetric without a shoulder (Fig. 12c). Also, a remarkable offset of the stresses on Ni and Fe atoms is observed. This offset suggests that each Fe atom in the disordered Ni-Fe solid solution can be considered a local perturbation and a stress concentrator. Such perturbations in the disordered Ni₃Fe particles cause significant local stress fluctuations. As a result, the CRSS required for dislocation nucleation at critical sites can be reached at lower average

The behavior of ordered Ni₃Fe particles is very different from that of disordered particles. The ordered arrangement of Fe atoms suppresses the spatial stress fluctuations and reveals the shoulder at high compressive stresses similar to the one in pure Ni (Fig. 12b). The suppressed stress fluctuations can explain why the simulated ordered Ni₃Fe particles are stronger than the disordered ones.

It should be noted the virial stress on an individual atom is a physically ambiguous quantity. Only the virial expression averaged over atomic groups gives the proper stress tensor. The stress

distribution maps discussed in our previous work included coarsegraining of the virial over atomic groups and thus represented the true stresses and stress gradients inside the particle. In the present work, we chose to display histograms of atomic stresses computed separately for the Ni and Fe atoms. Such histograms conveniently represent the statistical fluctuations of the local atomic environments in the material. The proper stress histograms could be obtained by averaging the Ni and Fe stress histograms with the respective stoichiometric coefficients. The histograms obtained would reveal similar trends as discussed above, such as the peak broadening and the shoulders, and would lead to the same conclusions. Thus, even though the histograms in Fig. 12 do not represent the stress distributions directly, they demonstrate the existence and relative magnitude of the stress gradients existing inside the particles.

The prediction that the ordered Ni₃Fe particles are stronger than the disordered ones does not contradict the experimental results, which indicate that the ordered (100) Ni-27Fe particles are as weak as, or weaker than, the disordered (111) Ni-27Fe particles (Fig. 8). Such particles are only partially ordered and contain disordered regions alongside small regions of the ordered L12 phase. At the critical nucleation sites, the material can still be locally in a disordered state. Moreover, the misfitting ordered and disordered phases are themselves stress concentrators. In such partially ordered particles, the role of the intrinsic mechanical strength of the ordered phase is diminished, while the additional stress concentrators degrade the particle strength. In contrast, the simulations performed here did not have the capability to model the creation of a second-phase inclusion inside the particle. Since the atomic ordering and disordering processes require diffusive jumps by the vacancy-exchange mechanism, they lie outside the time scale accessible by MD simulations. On the other hand, the MC simulations readily create the thermodynamically equilibrium ordered and disordered states, but this is accomplished through an unphysical atom swapping process that circumvents the phase nucleation.

The proposed "precipitation softening" effect, together with the solid solution softening, is the likely cause of the anomalously low strength of the Ni-50Fe particles containing the Fe-rich surface precipitates. The solid solution softening alone cannot explain the CRSS drop of about an order of magnitude in these particles compared to pure Ni (Fig. 8).

7. Conclusions

The following conclusions can be drawn from the results of the present study:

- 1. We have fabricated faceted single-crystalline micro- and nanoparticles of Ni-20, 27, and 50 at.% Fe alloys employing solid state dewetting of thin Ni-Fe bilayers deposited on a sapphire substrate. The Ni-20Fe particles exhibit only (111) orientation with respect to the substrate. The Ni-27Fe and Ni-50Fe particles exhibit mixed populations of (111) and (100) orientations.
- 2. The equilibrium crystal shape of the Ni-Fe particles was found to be similar to the equilibrium crystal shape of pure Ni. Small (about 5 nm in size) finely dispersed precipitates of the ordered Ni₃Fe (L1₂ structure) phase were observed in (100) oriented Ni-27Fe particles, while the (111) oriented particles did not show any signs of long-range order. Small Fe-rich precipitates were observed at the edges and corners of the Ni-50Fe particles. Partial ordering in the Ni-27Fe and Ni-50Fe particles was confirmed by the (400) XRD peak splitting.
- 3. Mechanical properties of the particles were measured by insitu microcompression tests performed in the HRSEM em-

ploying a flat diamond punch. Most particles exhibited compression behavior typical for nucleation-controlled plasticity. Initial elastic deformation up to a high engineering strain of 0.1-0.25 was followed by an abrupt displacement burst. The critical stress of the plastic collapse of the Ni-Fe particles was significantly lower than that of the Ni particles of comparable size, confirming the solid solution softening effect. This softening effect increases with increasing Fe concentration in the particles. The particles of all chemical compositions and orientations exhibit a pronounced size effect on the strength, with smaller particles being stronger than the larger ones.

- 4. MD simulations of particle compression were performed for single-crystalline faceted particles of Ni and ordered and disordered Ni₃Fe. The alloying with Fe was found to decrease the CRSS of the particles, with the weakening effect being strongest for disordered Ni₃Fe particles. The solute weakening of the disordered Ni₃Fe particles is attributed to inhomogeneities of the local stress distribution.
- 5. While the MD simulations predict the L1₂-ordered Ni₃Fe particles to be stronger than disordered, the experiments reveal the opposite effect. The weakening found in the experiments is explained by only partial long-range order in the Ni₃Fe particles and the existence of small precipitates causing stress concentrations and premature dislocation nucleation. This weakening was most significant in Ni-50Fe particles due to the synergistic action of the solid solution and precipitation weakening effects.

Finally, the results of the present work confirm that alloying with a second chemical component and precipitation of a second phase in defect-free metal nanostructures have the opposite effects on the strength than in bulk metallic alloys.

Declaration of Competing Interest

The authors declare that they have no known competing financial interests or personal relationships that could have appeared to influence the work reported in this paper.

Acknowledgemennts

A.S., O.M., A.B. and E.R. wish to thank the US-Israel Bi-National Science Foundation (joint BSF-NSF grant No. 2018625) for support. Y. M. acknowledges support from the National Science Foundation, Award No. 1904428. Helpful discussions with Prof. Dan Mordehai and Dr. Oleg Kovalenko, and assistance of Ms. Sasha Khalfin and Ms. Maayan Nidam with AFM measurements and data processing are heartily appreciated.

Supplementary materials

Supplementary material associated with this article can be found, in the online version, at doi:10.1016/j.actamat.2022.118527.

References

- E. Arzt, Size effects in materials due to microstructural and dimensional constraints: a comparative review, Acta Mater 46 (1998) 5611–5626, doi:10.1016/ S1359-6454(98)00231-6.
- [2] M.D. Uchic, D.M. Dimiduk, J.N. Florando, W.D. Nix, Sample dimensions influence strength and crystal plasticity, Science 305 (2004) 986–989, doi:10.1126/science.1098993.
- [3] Y. Choi, K.J. van Vliet, J. Li, S. Suresh, Size effects on the onset of plastic deformation during nanoindentation of thin films and patterned lines, J. Appl. Phys. 94 (2003) 6050–6058, doi:10.1063/1.1615702.
- [4] D. Mordehai, S.-W. Lee, B. Backes, D.J. Srolovitz, W.D. Nix, E. Rabkin, Size effect in compression of single-crystal gold microparticles, Acta Mater 59 (2011) 5202–5215, doi:10.1016/j.actamat.2011.04.057.

- [5] J.R. Greer, W.D. Nix, Nanoscale gold pillars strengthened through dislocation starvation, Phys. Rev. B. 73 (2006) 245410, doi:10.1103/PhysRevB.73.245410.
- [6] E. Rabkin, D.J. Srolovitz, Onset of plasticity in gold nanopillar compression, Nano Lett 7 (2007) 101–107, doi:10.1021/nl0622350.
- [7] Y. Feruz, D. Mordehai, Towards a universal size-dependent strength of facecentered cubic nanoparticles, Acta Mater 103 (2016) 433–441, doi:10.1016/j. actamat.2015.10.027.
- [8] A. Cao, E. Ma, Sample shape and temperature strongly influence the yield strength of metallic nanopillars, Acta Mater 56 (2008) 4816–4828, doi:10.1016/ j.actamat.2008.05.044.
- [9] R. Kositski, D. Mordehai, Role of dislocation pile-ups in nucleation-controlled size-dependent strength of Fe nanowires, Acta Mater 136 (2017) 190–201, doi:10.1016/j.actamat.2017.06.057.
- [10] S.J. Wang, H. Wang, K. Du, W. Zhang, M.L. Sui, S.X. Mao, Deformation-induced structural transition in body-centred cubic molybdenum, Nat. Commun. 5 (2014) 3433, doi:10.1038/ncomms4433.
- [11] R. Thevamaran, C. Griesbach, S. Yazdi, M. Ponga, H. Alimadadi, O. Lawal, S.J. Jeon, E.L. Thomas, Dynamic martensitic phase transformation in singlecrystal silver microcubes, Acta Mater 182 (2020) 131–143, doi:10.1016/j. actamat 2019 10 006
- [12] L. Zou, C. Yang, Y. Lei, D. Zakharov, J.M.K. Wiezorek, D. Su, Q. Yin, J. Li, Z. Liu, E.A. Stach, J.C. Yang, L. Qi, G. Wang, G. Zhou, Dislocation nucleation facilitated by atomic segregation, Nat. Mater. 17 (2017) 56–63, doi:10.1038/nmat5034.
- [13] J. Shin, L.Y. Chen, U.T. Sanli, G. Richter, S. Labat, M.-I. Richard, T. Cornelius, O. Thomas, D.S. Gianola, Controlling dislocation nucleation-mediated plasticity in nanostructures via surface modification, Acta Mater 166 (2019) 572–586, doi:10.1016/j.actamat.2018.12.048.
- [14] A. Sharma, J. Amodeo, N. Gazit, Y. Qi, O. Thomas, E. Rabkin, When more is less: plastic weakening of single crystalline Ag nanoparticles by the polycrystalline Au shell, ACS Nano 15 (2021) 14061–14070, doi:10.1021/acsnano.1c02976.
- [15] H. Bei, S. Shim, M.K. Miller, G.M. Pharr, E.P. George, Effects of focused ion beam milling on the nanomechanical behavior of a molybdenum-alloy single crystal, Appl. Phys. Lett. 91 (2007) 111915, doi:10.1063/1.2784948.
- [16] S.-W. Lee, D. Mordehai, E. Rabkin, W.D. Nix, Effects of focused-ion-beam irradiation and prestraining on the mechanical properties of FCC Au microparticles on a sapphire substrate, J. Mater. Res. 26 (2011) 1653–1661, doi:10.1557/jmr. 2011.221.
- [17] R. Maaß, L. Meza, B. Gan, S. Tin, Julia.R. Greer, Ultrahigh strength of Dislocation-Free Ni₃Al nanocubes, Small 8 (2012) 1869–1875, doi:10.1002/smll. 201102603.
- [18] C. Griesbach, S.-J. Jeon, D.F. Rojas, M. Ponga, S. Yazdi, S. Pathak, N. Mara, E.L. Thomas, R. Thevamaran, Origins of size effects in initially dislocationfree single-crystal silver micro- and nanocubes, Acta Mater 214 (2021) 117020, doi:10.1016/j.actamat.2021.117020.
- [19] A. Sharma, J. Hickman, N. Gazit, E. Rabkin, Y. Mishin, Nickel nanoparticles set a new record of strength, Nat. Commun. 9 (2018) 4102, doi:10.1038/ s41467-018-06575-6.
- [20] A. Sharma, R. Kositski, O. Kovalenko, D. Mordehai, E. Rabkin, Giant shape- and size-dependent compressive strength of molybdenum nano- and microparticles, Acta. Mater. 198 (2020) 72-84, doi:10.1016/j.actamat.2020.07.054.
- [21] A. Sharma, N. Gazit, L. Klinger, E. Rabkin, Pseudoelasticity of metal nanoparticles is caused by their ultrahigh strength, Adv. Func. Mater. 30 (2020) 1807554, doi:10.1002/adfm.201807554.
- [22] D. Guo, G. Xie, J. Luo, Mechanical properties of nanoparticles: basics and applications, J. Phys. D. Appl. Phys. 47 (2014) 013001, doi:10.1088/0022-3727/47/1/1013001
- [23] D. Kilymis, C. Gérard, J. Amodeo, U.V. Waghmare, L. Pizzagalli, Uniaxial compression of silicon nanoparticles: an atomistic study on the shape and size effects, Acta Mater 158 (2018) 155–166, doi:10.1016/j.actamat.2018.07.063.
- [24] D. Chachamovitz, D. Mordehai, The Stress-dependent activation parameters for dislocation nucleation in molybdenum nanoparticles, Sci. Rep. 8 (2018) 3915, doi:10.1038/s41598-018-21868-y.
- [25] J. Zimmerman, A. Bisht, Y. Mishin, E. Rabkin, Size and shape effects on the strength of platinum nanoparticles, J. Mater. Sci. 56 (2021) 18300–18312, doi:10.1007/s10853-021-06435-7.
- [26] J. Amodeo, K. Lizoul, Mechanical properties and dislocation nucleation in nanocrystals with blunt edges, Mater. Des. 135 (2017) 223–231, doi:10.1016/ i.matdes.2017.09.009.
- [27] K. Durst, O. Franke, A. Böhner, M. Göken, Indentation size effect in Ni–Fe solid solutions, Acta mater 55 (2007) 6825–6833, doi:10.1016/j.actamat.2007.08.044.
- [28] A. Suzuki, H. Inui, T.M. Pollock, L12 -strengthened cobalt-base Superalloys, Annu. Rev. Mater. Res. 45 (2015) 345–368, doi:10.1146/annurev-matsci-070214-021043.
- [29] A.H. Chokshi, A. Rosen, J. Karch, H. Gleiter, On the validity of the hall-petch relationship in nanocrystalline materials, Scr. Metall. 23 (1989) 1679–1683, doi:10.1016/0036-9748(89)90342-6.
- [30] K. Lu, L. Lu, S. Suresh, Strengthening materials by engineering coherent internal boundaries at the nanoscale, Science 324 (2009) 349–352, doi:10.1126/ science.1159610.
- [31] K. Lu, Making strong nanomaterials ductile with gradients, Science 345 (2014) 1455–1456, doi:10.1126/science.1255940.
- [32] J. Azadmanjiri, C.C. Berndt, A. Kapoor, C. Wen, Development of surface nanocrystallization in alloys by surface mechanical attrition treatment (SMAT), Crit. Rev. Solid State Mater. Sci. 40 (2015) 164–181, doi:10.1080/10408436.2014. 978446.

- [33] A. Bisht, R.K. Koju, Y. Qi, J. Hickman, Y. Mishin, E. Rabkin, The impact of alloying on defect-free nanoparticles exhibiting softer but tougher behaviour, Nat. commun. 12 (2021) 2515. doi:10.1038/s41467-021-22707-x.
- [34] P. Herre, J. Will, M. Dierner, D. Wang, T. Yokosawa, T. Zech, M. Wu, T. Przy-billa, S. Romeis, T. Unruh, W. Peukert, E. Spiecker, Rapid fabrication and interface structure of highly faceted epitaxial Ni-Au solid solution nanoparticles on sapphire, Acta Mater 220 (2021) 117318, doi:10.1016/j.actamat.2021.
- [35] D.N. Seidman, E.A. Marquis, D.C. Dunand, Precipitation strengthening at ambient and elevated temperatures of heat-treatable Al(Sc) alloys, Acta Mater 50 (2002) 4021–4035, doi:10.1016/S1359-6454(02)00201-X.
- [36] R.S. Irani, R.W. Cahn, Order-hardening of CuPt, Acta Metall 21 (1973) 575–584, doi:10.1016/0001-6160(73)90065-5.
- [37] G.W. Ardley, On the effect of ordering upon the strength of Cu_3Au , Acta Metall 3 (1955) 525–532, doi:10.1016/0001-6160(55)90110-3.
- [38] K. Shreiber, D. Mordehai, Dislocation-nucleation-controlled deformation of Ni₃Al nanocubes in molecular dynamics simulations, Model. Simul. Mater. Sci. Eng. 23 (2015) 085004, doi:10.1088/0965-0393/23/8/085004.
- [39] J. Schloesser, J. Rösler, D. Mukherji, Deformation behaviour of freestanding single-crystalline Ni 3Al-based nanoparticles, Int. J. Mater. Res. 102 (2011) 532– 537, doi:10.3139/146.110504.
- [40] L.J. Swartzendruber, V.P. Itkin, C.B. Alcock, The Fe-Ni (iron-nickel) system, J. Phase Equilibria 12 (1991) 288–312, doi:10.1007/BF02649918.
- [41] Y. Calvayrac, M. Fayard, Structural state and mechanical properties of polycrystalline, Ni3Fe Alloys Phys. Status Solidi. 17 (1973) 407–421, doi:10.1002/PSSA. 2210170204.
- [42] D. Amram, L. Klinger, E. Rabkin, Phase transformations in Au(Fe) nano-and microparticles obtained by solid state dewetting of thin Au-Fe bilayer films, Acta Mater 61 (2013) 5130–5143, doi:10.1016/j.actamat.2013.04.062.
- [43] Y. Mishin, M.J. Mehl, D.A. Papaconstantopoulos, Phase stability in the Fe-Ni system: Investigation by first-principles calculations and atomistic simulations, Acta Mater 53 (2005) 4029–4041, doi:10.1016/j.actamat.2005.05.001.
- [44] S. Plimpton, Fast parallel algorithms for short-range molecular dynamics, J. Comput. Phys. 117 (1995) 1–19, doi:10.1006/jcph.1995.1039.
- [45] V.I. Yamakov, Parallel Grand Canonical Monte Carlo (ParaGrandMC) Simulation Code, NASA Report NASA/CR-2016-219202, (2016).
- [46] A. Stukowski, Visualization and analysis of atomistic simulation data with OVITO-the Open Visualization Tool, Model. Simul. Mater. Sci. Eng. 18 (2010) 015012, doi:10.1088/0965-0393/18/1/015012.
- [47] B. Million, J. Růžičková, J. Velíšek, J. Vřešťál, Diffusion processes in the Fe-Ni system, Mater. Sci. Eng. 50 (1981) 43–52, doi:10.1016/0025-5416(81)90084-7.
- [48] A. Sharma, A. Kumar, N. Gazit, D.J. Srolovitz, E. Rabkin, Grain growth and solid-state dewetting of Bi-Crystal Ni-Fe thin films on sapphire, Acta Mater 168 (2019) 237–249, doi:10.1016/j.actamat.2019.02.015.
- [49] M. Wojdyr, Fityk: a general-purpose peak fitting program, J. Appl. Crystallogr. 43 (2010) 1126–1128, doi:10.1107/S0021889810030499.
- [50] H. Meltzman, D. Chatain, D. Avizemer, T.M. Besmann, W.D. Kaplan, The equilibrium crystal shape of nickel, Acta Mater 59 (2011) 3473–3483, doi:10.1016/j.actamat.2011.02.021.
- [51] R.V. Zucker, D. Chatain, U. Dahmen, S. Hagège, W.C. Carter, New software tools for the calculation and display of isolated and attached interfacial-energy minimizing particle shapes, J. Mater. Sci. 47 (2012) 8290–8302, doi:10.1007/ s10853-012-6739-x.
- [52] J. Frenkel, Zur Theorie der Elastizitätsgrenze und der Festigkeit kristallinischer Körper, Z. Phys. 37 (1926) 572–609, doi:10.1007/BF01397292.
- [53] Y.-L. Liu, Y. Zhang, H.-B. Zhou, G.-H. Lu, M. Kohyama, Theoretical strength and charge redistribution of fcc Ni in tension and shear, J. Phys. Condens. Matter 20 (2008) 335216, doi:10.1088/0953-8984/20/33/335216.
- [54] C.V. Thompson, Solid-state dewetting of thin films, Annu. Rev. Mater. Res. 42 (2012) 399–434, doi:10.1146/annurev-matsci-070511-155048.
- [55] A. Sharma, D.J. Srolovitz, E. Rabkin, to be published (2022).
- [56] C.M. Müller, R. Spolenak, Determination of the Au/SiNx interfacial energy by AFM and FIB tomography, Surf. Sci. 617 (2013) 94–105, doi:10.1016/j.susc.2013. 07.001.
- [57] W.W. Mullins, G.S. Rohrer, Nucleation barrier for volume-conserving shape changes of faceted crystals, J. Am. Ceram. Soc. 83 (2000) 214–216, doi:10.1111/ j.1151-2916.2000.tb01173.x.
- [58] L. Vitos, A.V. Ruban, H.L. Skriver, J. Kollár, The surface energy of metals, Surf. Sci. 411 (1998) 186–202, doi:10.1016/S0039-6028(98)00363-X.
- [59] E. Poirier, F.E. Pinkerton, R. Kubic, R.K. Mishra, N. Bordeaux, A. Mubarok, L.H. Lewis, J.I. Goldstein, R. Skomski, K. Barmak, Intrinsic magnetic properties of L10 FeNi obtained from meteorite NWA 6259, J. Appl. Phys. 117 (2015) 17E318, doi:10.1063/1.4916190.
- [60] N. Gazit, L. Klinger, E. Rabkin, Chemically-induced solid-state dewetting of thin Au films, Acta Mater 129 (2017) 300–311, doi:10.1016/j.actamat.2017.02.054.
- [61] O. Kovalenko, F.O. Chikli, E. Rabkin, The equilibrium crystal shape of iron, Scr. Mater. 123 (2016) 109–112, doi:10.1016/j.scriptamat.2016.06.006.
- [62] H. Meltzman, D. Mordehai, W.D. Kaplan, Solid-solid interface reconstruction at equilibrated Ni-Al₂O₃ interfaces, Acta Mater 60 (2012) 4359–4369, doi:10. 1016/j.actamat.2012.04.037.
- [63] R. Lipowsky, Surface-induced order and disorder: Critical phenomena at first-order phase transitions, J. Chem. Phys. 55 (1984) 2485–2490, doi:10.1063/1. 333703.
- [64] Y. Teraoka, Order-disorder transitions in binary alloys with the fcc (100) surface, Vacuum 41 (1990) 457–459, doi:10.1016/S0042-207X(05)80150-2.